Journal of Nanobiotechnology

RESEARCH Open Access

A nanoscale visual exploration of the pathogenic effects of bacterial extracellular vesicles on host cells

Minjae Kang[1†], Min Jeong Kim[1†], Dokyung Jeong[1], Hyung-Jun Lim[1], Ga-eun Go[1], Uidon Jeong[1], Eunyoung Moon[2], Hee-Seok Kweon[2], Nae-Gyu Kang[3], Seung Jin Hwang[3], Sung Hun Youn[3], Bo Kyoung Hwang[3] and Doory Kim[1,4,5,6*]

Abstract

Background Bacterial extracellular vesicles (EVs) are pivotal mediators of intercellular communication and influence host cell biology, thereby contributing to the pathogenesis of infections. Despite their significance, the precise effects of bacterial EVs on the host cells remain poorly understood. This study aimed to elucidate ultrastructural changes in host cells upon infection with EVs derived from a pathogenic bacterium, *Staphylococcus aureus* (*S. aureus*).

Results Using super-resolution fluorescence microscopy and high-voltage electron microscopy, we investigated the nanoscale alterations in mitochondria, endoplasmic reticulum (ER), Golgi apparatus, lysosomes, and microtubules of skin cells infected with bacterial EVs. Our results revealed significant mitochondrial fission, loss of cristae, transformation of the ER from tubular to sheet-like structures, and fragmentation of the Golgi apparatus in cells infected with *S. aureus* EVs, in contrast to the negligible effects observed following *S. epidermidis* EV infection, probably due to the pathogenic factors in *S. aureus* EV, including protein A and enterotoxin. These findings indicate that bacterial EVs, particularly those from pathogenic strains, induce profound ultrastructural changes of host cells that can disrupt cellular homeostasis and contribute to infection pathogenesis.

Conclusions This study advances the understanding of bacterial EV-host cell interactions and contributes to the development of new diagnostic and therapeutic strategies for bacterial infections.

Keywords Extracellular vesicle, Bacterial EV, Super-resolution fluorescence microscopy, Cristae loss

Introduction

Bacterial extracellular vesicles (EVs) are small membrane-bound structures released by bacteria into their environment [1, 2]. They are similar to the extracellular vesicles produced by eukaryotic cells and, like their eukaryotic counterparts, can transport various types of cargo molecules, including nucleic acids, proteins, lipids, viruses, enzymes, and toxins [2, 3]. Bacterial EVs have been shown to play a role in bacterial communication and transfer of genetic material, and they have been studied as potential diagnostic markers and therapeutic targets for bacterial infections [4]. Recently, a direct interaction

†Minjae Kang and Min Jeong Kim contributed equally to this work.

*Correspondence:
Doory Kim
doorykim@hanyang.ac.kr
[1]Department of Chemistry, Hanyang University, Seoul 04763, Republic of Korea
[2]Electron Microscopy Research Center, Korea Basic Science Institute, Cheongju 28119, Republic of Korea
[3]R&D Center, LG H&H Co., Ltd, Seoul 07795, Republic of Korea
[4]Research Institute for Convergence of Basic Science, Hanyang University, Seoul 04763, Republic of Korea
[5]Institute of Nano Science and Technology, Hanyang University, Seoul 04763, Republic of Korea
[6]Research Institute for Natural Sciences, Hanyang University, Seoul 04763, Republic of Korea

between bacterial EVs and human hosts was revealed [5]. For example, recent research has shown internalization of gram-positive bacterial EVs by eukaryotic cells, such as epithelial and macrophage cell lines, via endocytosis [5–8]. Additionally, fusion of bacterial EVs with cell membranes of eukaryotic cells has also been demonstrated [9]. However, the effects of bacterial EVs on host cells are not yet understood at a higher level. To investigate these effects, it is crucial to observe the ultrastructural changes in host cells in response to bacterial EV infection.

Since the role of EVs can to a large extent be determined by the type of cargo, EVs derived from different types of bacteria are expected to exhibit distinct bioactivities in host cells. For example, *Staphylococcus aureus* (*S. aureus*) produces EVs containing several virulence factors, such as exotoxins and enzymes, which could possibly aid in its pathogenesis [10]. Thus, *S. aureus* is considered a pathogenic bacterium that can cause a wide range of infections, including skin infections (such as boils, impetigo, and folliculitis), respiratory infections (such as pneumonia and sinusitis), and systemic infections (such as sepsis and endocarditis) [11]. In contrast, *Staphylococcus epidermidis* (*S. epidermidis*), another type of bacterium commonly found on the skin and nose of humans, is considered a commensal bacterium and is usually considered to be less virulent than *S. aureus*. Therefore, EVs produced by different types of bacteria can affect host cells in different ways. If such subtle ultrastructural changes in host cells during bacterial EV-mediated infection can be detected, this could represent a useful diagnostic approach for assessing bacterial infection.

To address this, we investigated the ultrastructural changes in various organelles of host cells during bacterial EV-mediated infection. The effects of different bacterial EVs on host cells were investigated using EVs produced by different types of bacteria, including the pathogenic *S. aureus* and the relatively non-pathogenic *S. epidermidis*. To observe the nanoscale ultrastructural changes in host cells, we mainly employed super-resolution fluorescence microscopy [12–14], stochastic optical reconstruction microscopy (STORM) [15], for host cells infected with bacterial EVs at different times, and we quantified the ultrastructural changes in each organelle, including the mitochondria, endoplasmic reticulum (ER), Golgi, lysosome, and microtubule. To confirm these observations, we also employed transmission electron microscopy (TEM) and high-voltage electron microscopy (HVEM), and we compared the results. In this systematic investigation, using advanced microscopic techniques, we observed significant changes in the mitochondria, ER, Golgi apparatus, lysosome, and microtubule during pathogenic bacterial EV-mediated host cell infection, which have not been previously reported. Further investigation into the distinct components in *S. aureus* EVs compared to *S. epidermidis* EVs, which can induce harmful effects on host cells, revealed that the high amounts of enterotoxin and protein A in *S. aureus* EVs induce such pathogenic effects on host cells. Therefore, this study of the impact of bacterial EVs on host cells has unveiled new aspects of the infection pathway associated with bacterial pathogenesis and poses challenges and opportunities for providing innovative approaches to diagnosis and treatment.

Methods

Sample preparation for cell fluorescence imaging

The HaCaT cells (T0020001; AddexBio technologies) and HDF cells (ATCC, CRL-1635) were cultured in Dulbecco's modified Eagle's medium (DMEM) (LM 001–05; Welgene) supplemented with 1% (v/v) penicillin-streptomycin (15070; Thermo Fisher Scientific) and 10% (v/v) fetal bovine serum (FBS) (A31605; Thermo Fisher Scientific) at 37 °C with 5% CO_2 in a humidified incubator.

For fluorescence imaging, the cells were seeded on glass-bottom confocal dishes (100350; SPL Life Sciences) and incubated at 37 °C with 5% CO_2 for 24–48 h (1–2 days). The cells were then washed with prewarmed Dulbecco's phosphate-buffered saline (DPBS) (DPB 001; SolBio) and fixed for 10 min at room temperature (RT) with 3% (v/v) paraformaldehyde (PFA) (15714; Electron Microscopy Sciences) and 0.1% (v/v) glutaraldehyde (GA) (16020; Electron Microscopy Sciences) in DPBS, which is the widely optimized fixation condition for super-resolution fluorescence microscopy imaging of membranous structures, including mitochondria [16–20]. To quench autofluorescence from unreacted aldehydes, the fixed cells were immersed in freshly prepared 0.1% (w/v) $NaBH_4$ (16940-66-2; Sigma-Aldrich) for 7 min at RT. After washing in DPBS, the cells were permeabilized for 15 min at RT using 0.25% Triton X-100 (22140; Electron Microscopy Sciences) in DPBS. Following permeabilization, the cells were treated with blocking buffer containing 3% (w/v) bovine serum albumin (BSA) (CNB102-0100; CellNest) for 30 min at RT. The cells were then incubated with primary antibodies in blocking buffer for 30 min at RT followed by labeling with Alexa Fluor® (AF) 647- or 488-conjugated secondary antibodies in blocking buffer for 1 h at RT. After two washes with DPBS, the cells were postfixed for 10 min with 2% (v/v) PFA and 0.05% (v/v) GA in DPBS at RT. The following primary antibodies were used: rabbit polyclonal anti-TOM22 (ab246862; Abcam) to label the outer mitochondrial membrane, mouse monoclonal anti-ATPB to label the mitochondrial cristae, rabbit monoclonal anti-KLC3 (ab180523; Abcam) to label the endoplasmic reticulum (ER) structure, and mouse monoclonal anti-LAMP1 (ab25630; Abcam) to label the lysosome. Mouse monoclonal anti-GM130 (618022; BD Transduction

Laboratories) was used to label the Golgi apparatus and mouse monoclonal anti-acetylated tubulin antibody (T6793; Sigma-Aldrich) was utilized for acetylated tubulin. The secondary antibodies used were AF647-conjugated donkey anti-mouse IgG (A-31571; Thermo Fisher Scientific), AF647-conjugated donkey anti-rabbit IgG (A-31573; Thermo Fisher Scientific), and AF488-conjugated donkey anti-rabbit IgG (A-21206; Thermo Fisher Scientific). The cell nuclei were stained using Hoechst 33342 solution (62249; Thermo Fisher Scientific) diluted in DPBS for 10 min in a light-protected environment.

To treat cells with bacterial EVs, the seeded cells were first briefly washed with DMEM and subsequently incubated in cell culture media containing *S. aureus* or *S. epidermidis* EVs for 0.5, 4, 12, or 24 h. Purified EVs were provided in solution from the R&D Center of LG H&H, as described previously [21]. We treated the cells with EVs at a concentration of $7x10^7$ particles/mL for both *S. aureus* and *S. epidermidis* EVs. We chose this concentration because of substantial changes in the mitochondria, ER, and Golgi apparatus of *S. aureus* EV-treated cells starting from this concentration; there were no significant differences in organelle morphology compared with untreated control cells at concentrations less than $7x10^7$ particles/mL. To treat cells with protein A from *S. aureus* (P6031; Sigma-Aldrich), the seeded HaCaT cells were first washed with DPBS, and then, the cells were treated with 200 μL of protein A solution with a concentration of 5 μg/mL for 30 min. After treatment with bacterial EVs or protein A, the cells were washed with pre-warmed DPBS, followed by fixation, permeabilization, blocking, primary and secondary antibody labeling, and post-fixation, as described above.

Sample preparation for EV imaging

Purified EVs from *S. aureus* and *S. epidermidis* were imaged in a pre-washed glass-bottom confocal dish. The dish was sonicated in 1 M potassium hydroxide (KOH) (1310-58-3; Daejung) for 15 min, rinsed with distilled water, and exposed to UV light from a lamp for 15 min. The dish was then treated with 0.01% poly-L-lysine (PLL) solution (P4707; Sigma-Aldrich) for 15 min to promote EV attachment, rinsed twice with distilled water, and 200 μL of solution containing purified EVs at a concentration of 1.69×10^8 particles/mL was then added to the center of the dish and incubated for 30 min.

To immunolabel protein A and enterotoxin B of EVs, the EVs attached to the PLL-precoated glass-bottomed dishes were first incubated in 3% (w/v) BSA for 30 min. The EVs were then incubated with primary antibodies in blocking buffer for 30 min at RT followed by labeling with AF647-conjugated donkey anti-rabbit IgG in blocking buffer for 1 h at RT. The following primary antibodies were used: anti-*S .aureus* antibody (ab20920; Abcam) to label the protein A, *S .aureus* polyclonal antibody (PA1-7246; Thermo Fisher Scientific) to label enterotoxin B.

To label EVs with Nile red membrane dyes, the purified EVs were labeled with 3 nM Nile red membrane dye solution (415711000; Acros Organics) in DPBS for 30 min.

STORM imaging

To carry out STORM imaging of human skin cell samples, fluorophore-labeled cells were immersed in an imaging buffer composed of 100 mM cysteamine (30070; Sigma-Aldrich), 5% (w/v) glucose (50-99-7; Sigma-Aldrich), and oxygen-scavenging enzymes (0.5 mg/mL glucose oxidase [G2133; Sigma-Aldrich] and 38 μg/mL catalase [C3515; Sigma-Aldrich] in DPBS at pH 8.5) in DPBS at pH 8.5. STORM imaging was performed using a custom-built inverted microscope (Ti2-U; Nikon) equipped with a 100×1.49 NA oil-immersion objective lens (CFI SR HP Apo TIRF; Nikon) as previously described [22]. The prepared human skin cell sample was continuously illuminated by a 647 nm laser (120 mW, OBIS; Coherent) or a 488 nm laser (110 mW, OBIS; Coherent) to excite the fluorophores. Purified EV samples labeled with Nile red were illuminated continuously using a 561 nm laser (100 mW, OBIS; Coherent). When necessary, a 405 nm laser (0.1-1 mW, OBIS; Coherent) was used as an activation laser to reactivate the AF dyes from the dark state to the fluorescent state. Total internal reflection fluorescence illumination was applied, and the emitted fluorescence was passed through a bandpass emission filter (LF 408/488/561/635-B-000; Semrock). Filtered fluorescence was detected using an EMCCD camera (iXon Ultra 888; Andor) at a frame rate of 65 Hz. Throughout the STORM imaging process, the CRISP autofocus system (ASI) was used to maintain the focal plane by detecting a separate IR beam reflected from the sample-liquid interface through an objective lens.

Additionally, a cylindrical lens with a focal length of 500 mm (LJ1144RM-A; Thorlabs) was introduced for astigmatism to perform 3D STORM imaging (Center for Polymers and Composite Materials, Hanyang University, Korea). This lens created a cylindrical distortion, altering the focus differently along two orthogonal axes and resulting in elliptical rather than circular point spread functions (PSFs) [23]. This distortion facilitated the differentiation of axial and lateral positions of fluorescent molecules. The observed astigmatism enabled the reconstruction of 3D spatial information by analyzing the modified PSF from the collected data. By measuring the width of the PSF in the x and y directions, respectively, caused by the cylindrical lens, we could accurately determine the z-coordinate of each molecule, achieving high-resolution 3D imaging.

To perform two-color STORM imaging, beads in the same region of interest were first imaged in both the

647 nm and 488 nm channels to accurately match the different color channels. Then, AF 647-labeled cellular organelles in the samples were imaged first with an excitation laser of 647 nm. Subsequently, AF 488-labeled cellular organelles were imaged using a 488 nm excitation laser. These fluorescent signals were distinguished by the previously mentioned bandpass emission filter, which allowed for the separation of the different color channels.

To reconstruct the STORM images, each point spread function observed in the raw STORM movie was fitted to a Gaussian function to determine the centroid positions of the individual fluorophores. These centroids were then drift-corrected and used in the rendering process for STORM image reconstruction [15].

EM imaging

For TEM imaging, HaCaT keratinocytes were first fixed with 2.5% GA in 0.1 M cacodylate buffer (pH 7.4) overnight at 4 °C. The samples were then washed with cacodylate buffer. After washing, post-fixation was conducted with 1–2% osmium tetroxide in 0.1 M cacodylate buffer on ice for 1 h. After three washes with cacodylate buffer, the samples were dehydrated using a graded ethanol series, followed by progressive incubation with propylene oxide and Epon 812, and finally embedded in 100% Epon 812 resin. Ultrathin sections of approximately 70 nm were obtained using an EM UC7 ultramicrotome (Leica, Austria) and placed on 100–150 mesh copper grids. The ultrathin sections on the grids were stained with uranyl acetate and lead citrate, followed by imaging using a TEM (JEM-1400 Plus at 120 kV, JEOL, Japan).

For HVEM imaging, the samples were prepared in a similar manner but post-fixed using 1–2% osmium tetroxide and 1.5% potassium ferrocyanide in 0.1 M cacodylate buffer. Thick sections (approximately 700 nm thick) were obtained for 3D ultrastructural reconstruction. Imaging was performed using a KBSI Bio-HVEM (JEM-1000BEF at 1,000 kV, JEOL, Japan). A total of 60 tilt images from +60° to -60° tilting angles in increments of 2° were recorded using TEM Recorder software (JEOL System Technology, Tokyo, Japan). Alignment and reconstruction of these images were accomplished using Composer and Visualizer-Evo software (TEMography.com, Frontiers Inc., Tokyo, Japan). AMIRA software (Thermo Fisher Scientific (FEI), Hillsboro, OR, USA) was used for surface rendering and 3D modeling.

Image quantification

To measure the size of the purified EVs, each EV particle was first identified using the previously reported DBSCAN cluster analysis method [24]. After identifying each EV particle, a single-molecule distribution was generated for each particle, followed by fitting to a two-dimensional Gaussian function. In the fitted Gaussian function, the full width at half maximum (FWHM) was used as the diameter of each EV particle.

For quantification of the ultrastructure of each organelle, including mitochondria, ER, lysosomes, and the Golgi apparatus, we employed 'SR-Tesseler', a software that exploits the coordinates and intensity of localized molecules obtained through localization-based super-resolution techniques, including STORM [25]. The rendering process was conducted based on the intensity of localized molecules for enhanced visualization. After rendering, image quantification was performed individually for each cellular organelle as follows:

First, for the quantification of mitochondria, we employed the ImageJ software 'Mitochondria Analyzer' plug-in [26]. Individual mitochondria in the STORM images generated from the SR-Tesseler were identified using a skeletonization process, and the longest diameter and the number of branches for each identified mitochondrion were calculated.

To analyze the ultrastructure of the ER, 'AnalyzER' software implemented in MATLAB (The Mathworks) was employed [27]. With this program, the FWHM for both the maximum and minimum tubule widths were determined based on pixel-level intensity profiling, in which the range between these values was designated as the threshold for tubule width. The regions with FWHM values exceeding the maximum tubule width were classified as sheet structures, whereas those with FWHM values below the minimum tubule width were considered background signals. The regions within the threshold range were recognized as tubular structures. Using the images classified for each structure, we computed the ratio of the areas occupied by the sheet and tubular structures. The percentages of tubular and sheet-like structures were computed using ImageJ software, employing its area fraction measurement features.

For quantitative analysis of the radial distribution of the Golgi apparatus and lysosomes from the center of the nucleus, we utilized a custom-written MATLAB code. With this MATLAB code, the initial image processing was performed, involving median filtering and intensity filtering using Otsu's thresholding algorithm, as previously described [18]. After the initial image processing, each organelle in the images was identified by the boundaries of each object using 8-point connectivity and dilating them by 1 pixel. The Euclidean distances between the coordinates of the pixels contained in the lysosomes or Golgi and the coordinates of the cellular nucleus centroid were then used to determine the intracellular radial distribution.

Determination of spatial resolution in STORM imaging

To measure the spatial resolution of STORM images, we conducted Fourier ring correlation (FRC) analysis using

the corresponding ImageJ FRC plug-in. Our image acquisition included 50,000 frames per STORM image. These frames were split into two sets of 25,000 frames each, and the FRC was calculated between these two sets. Based on previous study [28], a correlation cut-off value of 1/7 was applied to determine the spatial resolution from the FRC analysis. This analysis was performed on five STORM images for each cellular organelle, and the resulting resolution values were averaged for a facilitate comparison across different organelles.

Results

The degradation of mitochondrial ultrastructures by EVs derived from *S. aureus*

To investigate the effects of bacterial EV on the ultrastructure of host cells, we chose *S. aureus* and *S. epidermidis* as pathogenic and relatively non-pathogenic bacterial sources, respectively. Thus, we first purified EVs from cultured *S. aureus* and *S. epidermidis* and performed STORM imaging to confirm the purified EVs by measuring their average membrane diameters. As shown in Fig. S1, the average diameters of the purified EVs from *S. aureus* and *S. epidermidis* were 110.6 and 114.7 nm, respectively, in the STORM images of Nile red-labeled EVs, which is consistent with the reported range for EVs [21, 29].

Because both *S. aureus* and *S. epidermidis* are commonly found in human skin [30], HaCaT keratinocytes were used as host cells for infection with bacterial EVs. Thus, we treated HaCaT cells with purified EVs from cultured *S. aureus* or *S. epidermidis* and then performed STORM imaging of mitochondria in the cells at various time points to examine the alterations in mitochondrial morphology. Mitochondrial dynamics play a crucial role in cellular homeostasis, and mitochondrial aberrations are often associated with various pathological conditions, including infectious diseases [31]. Therefore, we investigated the effects of *S. aureus* and *S. epidermidis* EVs on mitochondrial dynamics to better understand the potential pathogenic effects of these bacterial species. As shown in Fig. 1A and Fig. S2, STORM images revealed a striking difference in the mitochondrial morphologies between cells treated with *S. aureus* EVs versus those treated with *S. epidermidis* EVs. In particular, we observed pronounced mitochondrial fission in *S. aureus* EV-infected cells after 30 min of EV infection, whereas no such effect was observed in cells infected with *S. epidermidis* EVs. The induction of mitochondrial fission by *S. aureus* EV infection was also confirmed by quantitative analysis of mitochondrial length and the ratio of branched mitochondria measured from STORM images. As shown in Fig. 1B, a longer length of mitochondria and the ratio of branched mitochondria decreased in *S. aureus* EV-treated HaCaT cells, suggesting induction of mitochondrial fission. Mitochondrial fission and mitochondrial network fragmentation are well-known phenomena observed in virus-infected cells and aged skin, indicating a potential link between pathogenicity and alterations in mitochondrial dynamics [32–34]. Therefore, our results suggest that *S. aureus* EVs induce mitochondrial fission, which is a common pathogenic effect following viral infection.

We also observed induction of mitochondrial fission in skin cells following exposure to *S. aureus* EVs using TEM images. As shown in Fig. 1C, D, mitochondrial fission was observed in the skin cells treated with *S. aureus* EVs, which was not clearly observed in those treated with *S. epidermidis* EVs. However, the sectioned sample prepared for TEM imaging may not provide a complete view of the full-length mitochondrion, thus limiting the interpretation of the three-dimensional structure of the entire mitochondrion [35, 36]. To overcome this limitation, we performed HVEM imaging of 700 nm-thin sections of HaCaT cells treated with bacterial EVs. Interestingly, we observed unexpected phenomenon from the host cell treated with *S. aureus* EVs, in addition to mitochondria fission effect: the mitochondria in cells infected with *S. aureus* EVs exhibited a notable loss of cristae, whereas this effect was absent in *S. epidermidis* EV-infected and control cells (Fig. 2A, Movies S1–3). To confirm this, we also performed two-color STORM imaging of the outer membrane and cristae of mitochondria using specific markers for the translocase of the mitochondrial outer membrane (TOM22) and ATP synthase. As shown by the two-color STORM images in Fig. 2B, we also observed a loss of mitochondrial cristae in *S. aureus* EV-treated HaCaT cells, which is consistent with the HVEM images. To quantify the extent of cristae loss, the localization density of ATP synthase inside the mitochondria was measured. The quantification results in Fig. 2C clearly revealed degraded cristae in *S. aureus* EV-treated HaCaT cells, which were not observed in *S. epidermidis* EV-treated HaCaT cells. The observed loss of cristae in *S. aureus* EV-infected cells suggests a significant impact on cellular energy metabolism because cristae contain ATP synthase, which is a key enzyme involved in cellular energy production. Mitochondrial cristae are integral to the electron transport chain, which is crucial for ATP production. Therefore, their degradation indicates a disruption of energy homeostasis, potentially leading to impaired cellular functions and signaling pathways. Collectively, the observed loss of cristae following *S. aureus* EV infection may compromise ATP synthase function, thus suggesting a pathogenic effect associated with *S. aureus* EVs.

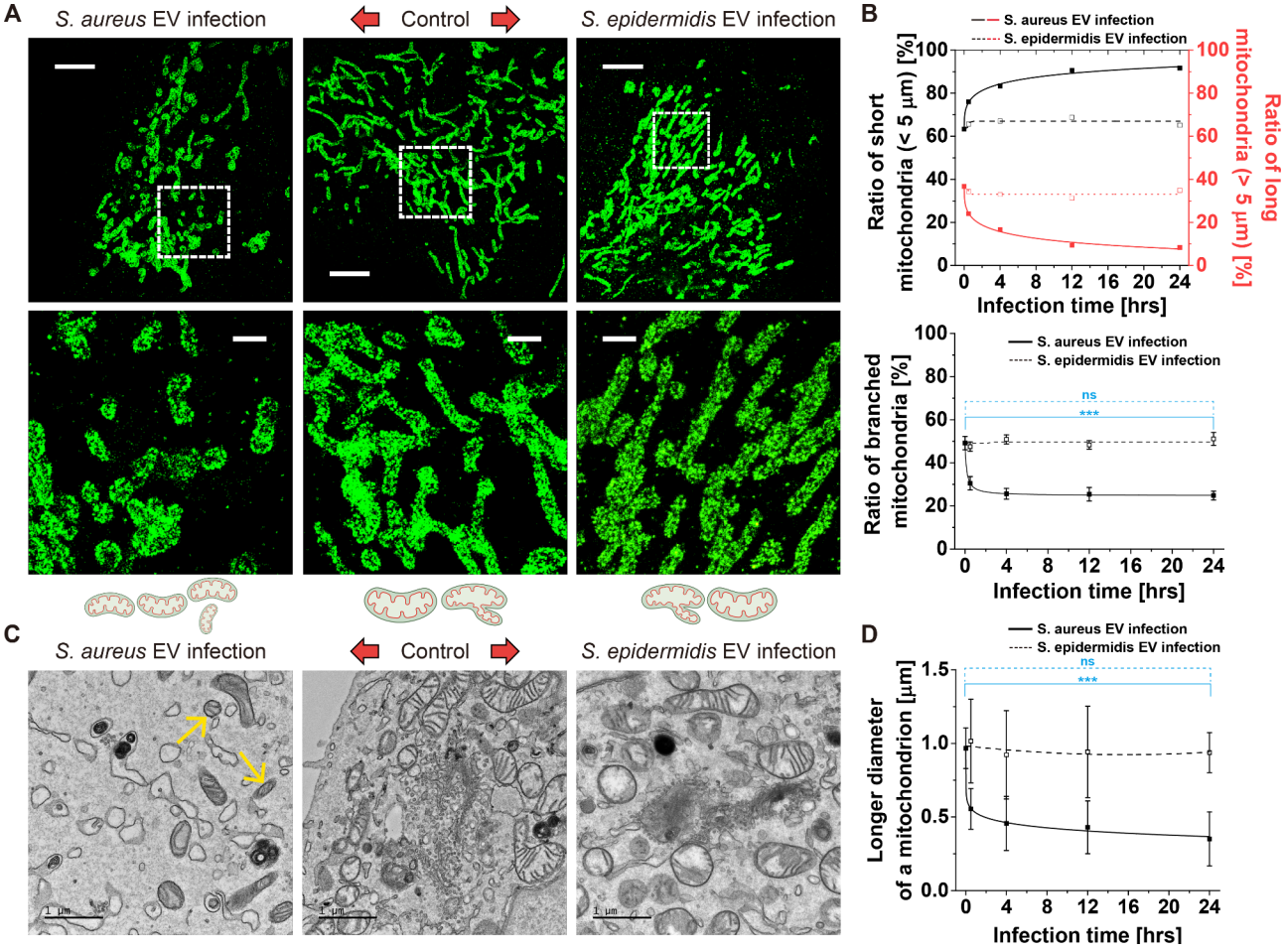

Fig. 1 Mitochondria fission effect of *S. aureus* EV-mediated infection. (**A**) Representative STORM images of mitochondria in epithelial keratinocyte (HaCaT) cells treated with *S. aureus* EVs (left) or *S. epidermidis* EVs (right) after 30 min of EV infection. Enlargement of the boxed region is shown at the bottom. Schematic diagrams are shown together. (**B**) Quantitative analysis of the mitochondrial ultrastructural changes in terms of the ratio of long (with > 5 μm longest diameter) and short mitochondria (with < 5 μm longest diameter) and ratio of branched mitochondria from STORM images. ($n = 10$, mean ± SD) (**C**) Representative TEM images of HaCaT cells treated with *S. aureus* (left) or *S. epidermidis* (right) EVs after 30 min of EV infection. Arrows: mitochondrial fission. (**D**) Quantitative analysis of the size of the mitochondria in terms of the longer diameter from TEM images. ($n = 10$, mean ± SD) (ns: $p > 0.05$, ***$p < 0.001$) Scale bars: (**A**) 5 μm (top), 1 μm (bottom). (**C**) 1 μm

The transformation from a tubular to a sheet-like endoplasmic reticulum structure by *S. aureus* EV treatment

Next, we investigated ultrastructural changes in the ER following treatment with different types of bacterial EVs. We performed STORM imaging of the ER of HaCaT cells treated with purified EVs from cultured *S. aureus* or *S. epidermidis*. As shown in Fig. 3A and Fig. S3, STORM images of the ER in HaCaT cells revealed two distinct morphological forms of ER: tubular and sheet-like structures. Interestingly, the balance between these two distinct forms varied depending on the type of bacterial EVs used for the infection. For example, in cells infected with *S. aureus* EVs, we observed a pronounced morphological shift from the tubular to sheet-like structure of the ER. However, this alteration was not evident in cells treated with *S. epidermidis* EVs. Such changes in global ER network topology and integrity are known to be key features associated with physiological and stress states [37]. To quantify the ratio of these two ER morphologies from STORM images, we employed the AnalyzER software program, which allows classification of ER structures [27]. As shown in Fig. 3B, quantitative measurements of the structural changes of the ER in response to each bacterial EV treatment revealed an increase in the sheet-like structure by *S. aureus* EV treatment and an increase in the tubular structure by *S. epidermidis* EV treatment.

The transformation from a tubular to a sheet-like ER configuration has been suggested to be associated with cellular responses to starvation, particularly during the autophagy process. This suggests that *S. aureus* EVs induce stress responses similar to those observed in nutrient-deprived cells, further emphasizing the deleterious effects of *S. aureus* EVs on cellular homeostasis. In particular, it has recently been reported that

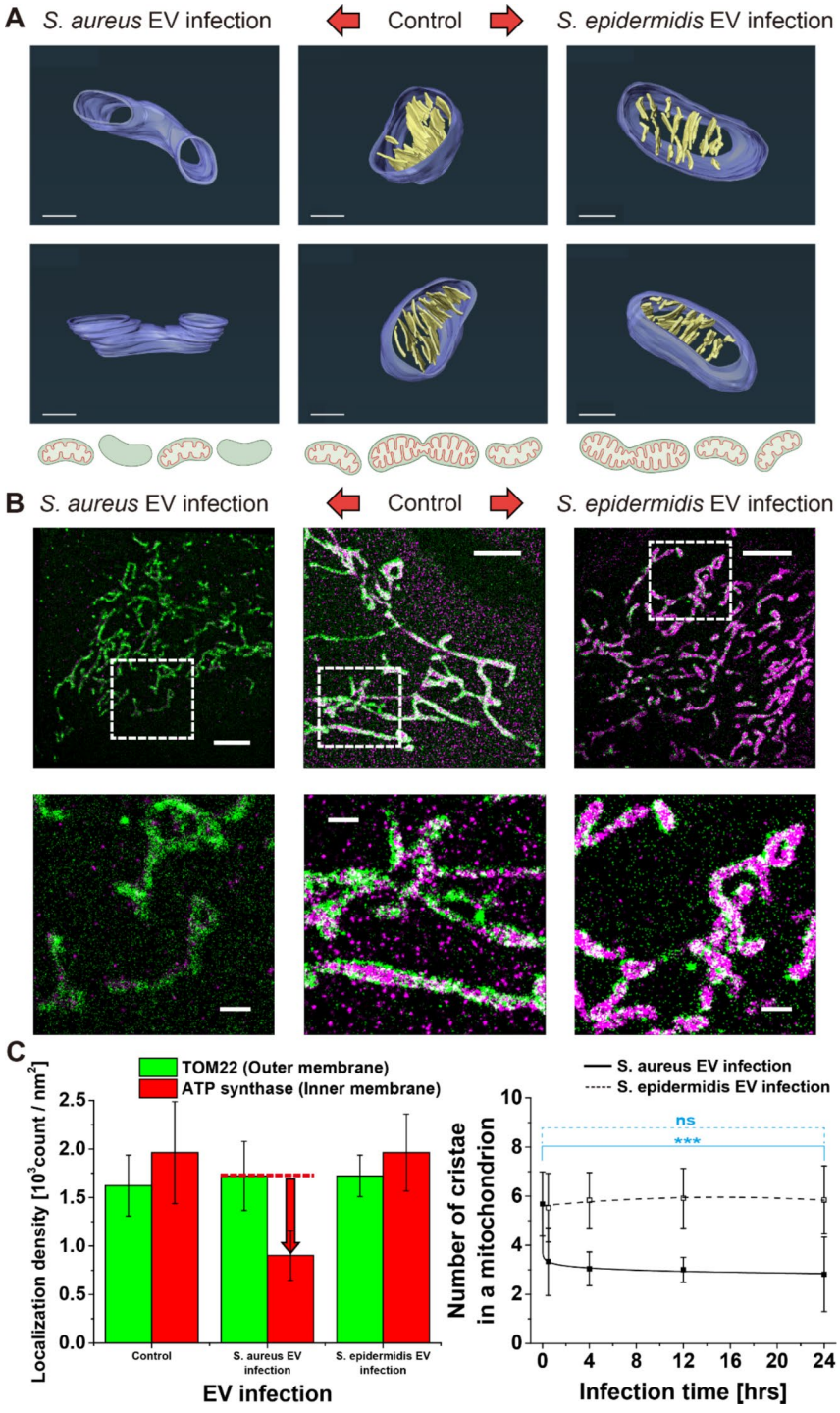

Fig. 2 Loss of cristae by *S. aureus* EV infection. (**A**) 3D reconstructed HVEM images of epithelial keratinocyte (HaCaT) cells treated with *S. aureus* (left) or *S. epidermidis* (right) EVs after 30 min of EV infection at different angles, showing the loss of cristae by *S. aureus* EV infection. Schematic diagrams are shown together. (**B**) Representative two-color STORM images showing the outer membrane protein TOM22 of mitochondria (green) and cristae immunolabeled for ATP synthase (magenta) in HaCaT cells treated with *S. aureus* (left) or *S. epidermidis* (right) EVs after 30 min of EV infection. Enlargement of the boxed region is shown together at the bottom. (**C**) Quantitative analysis of the outer membrane protein and cristae using their mean localization densities in a mitochondrion from STORM images ($n = 10$, mean ± SD) and for the number of cristae in a mitochondrion from TEM images. ($n = 10$, mean ± SD) (ns: $p > 0.05$, ***$p < 0.001$) Scale bars: (**A**) 300 nm. (**B**) 5 μm (top), 1 μm (bottom)

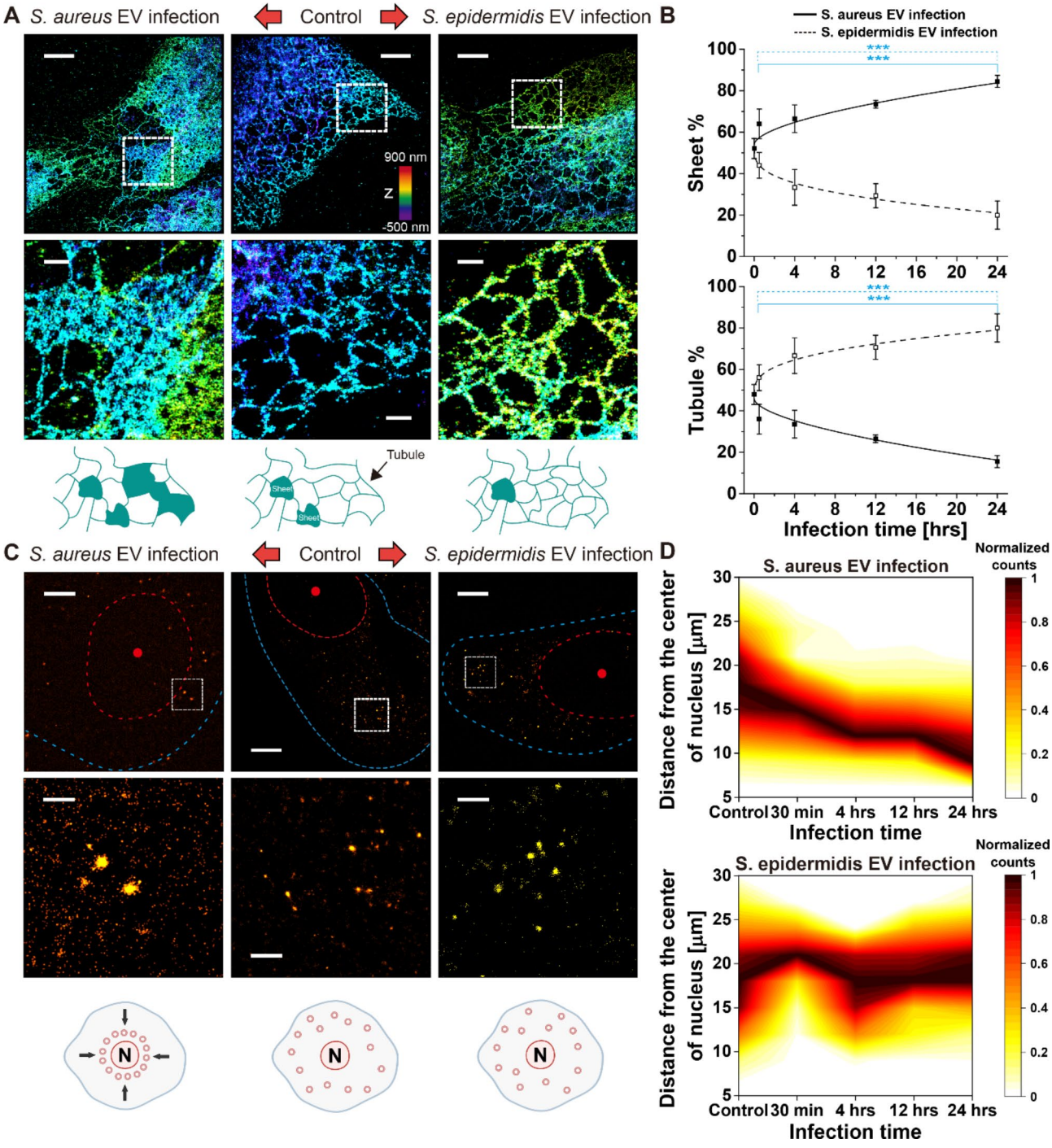

Fig. 3 Transformation of endoplasmic reticulum (ER) between sheet and tubular structures by EV infection. (**A**) Representative STORM images of ER in epithelial keratinocyte (HaCaT) cells treated with *S. aureus* EVs (left) or *S. epidermidis* EVs (right) after 30 min of EV infection. Enlargement of the boxed region is shown at the bottom. Schematic diagrams are shown together. (**B**) Quantitative analysis of the ultrastructural changes of the ER in terms of the percentage of sheet-like and tubular structures. ($n = 10$, mean ± SD) (**C**) Representative STORM images of lysosomes in HaCaT cells treated with *S. aureus* EVs (left) or *S. epidermidis* EVs (right) after 30 min of EV infection. Enlargement of the boxed region is shown together at the bottom. Schematic diagrams are shown together. Dashed lines: cell membrane boundary (blue) and nucleus boundary (red). (**D**) Quantitative analysis of the radial distribution of lysosomes from the center of the nucleus. ($n = 10$) (ns: $p > 0.05$, ***$p < 0.001$) Scale bars: (**A**) 5 μm (top), 1 μm (bottom). (**C**) 5 μm (top), 1 μm (bottom)

ER morphology is actively regulated by lysosomes in response to nutritional status [38]. For example, Meng et al. found that the induction of autophagy in starved cells resulted in the accumulation of lysosomes in perinuclear regions followed by a decrease in ER tubules in the cell periphery and a concomitant increase in sheet content in central regions of the cell. As we observed a similar transformation from a tubular to a sheet-like ER structure in HaCaT cells treated with *S. aureus* EVs, we performed STORM imaging of lysosomes to assess whether *S. aureus* EV-treated HaCaT cells exhibited this nutrient-depletion condition (Fig. 3C, Fig. S4). Interestingly, we observed accumulation of lysosomes in the perinuclear regions of HaCaT cells treated with *S. aureus* EVs but not in *S. epidermidis* EV-treated or non-treated HaCaT cells, suggesting that *S. aureus* EV-treated HaCaT cells experienced nutrient depletion (Fig. 3D). We also performed two-color STORM imaging of ER and lysosomes at different time points. As shown in Fig. S5, two-color STORM images of ER and lysosomes indicate that changes in both organelles occur simultaneously, beginning approximately 30 min post-infection and progressing at similar rates. This aligns with the previously published literature, suggesting that lysosomal positioning influences ER tubule elongation and connectivity. Therefore, we observed that ER reshaping was regulated by lysosomal positioning in response to pathogenic *S. aureus* EV treatment, similar to the autophagy process in nutrient-depleted cells, suggesting that *S. aureus* appears to employ pathogenic mechanisms.

The fragmentation and dispersal of the Golgi apparatus by treatment of EV derived from pathogenic *S. aureus*

Finally, we used STORM imaging to examine the Golgi apparatus in cells exposed to EVs from *S. aureus* or *S. epidermidis*. The Golgi apparatus typically appears as a series of stacked, flat, and ribbon-like structures located near the nucleus. We observed a normal Golgi appearance in control HaCaT cells that were not treated with any bacterial EVs (Fig. 4A, Fig. S6). However, in cells infected with *S. aureus* EVs, we detected clear fragmentation and dispersion of the Golgi complex from the nucleus, a phenomenon that was absent in cells treated with *S. epidermidis* EVs. This fragmentation and mislocalization of the Golgi apparatus from its typical perinuclear location is reminiscent of the cellular alterations observed in response to stress or damage, such as in coronavirus-infected cells, suggesting that a similar pathogenic mechanism may be at play with *S. aureus* EVs [39]. To further confirm the changes in the Golgi apparatus in the time series, we quantified the number of Golgi fragments and the radial distribution from the nucleus in the STORM images. As shown in Fig. 4B, the number of Golgi fragments increased to 205% after *S. aureus* EV infection over 24 h, whereas it remained relatively constant (110%) after *S. epidermidis* EV infection. Additionally, we observed that the center of mass of the Golgi apparatus relative to the center of the nucleus approximately doubled (221%) following *S. aureus* EV infection, whereas it remained constant following *S. epidermidis* EV infection. To confirm this observation, we performed HVEM imaging of the Golgi apparatus in HaCaT cells. As shown in Fig. 4C and Movies S4–6, 3D reconstructed HVEM images of HaCaT cells treated with *S. aureus* EVs revealed fragmentation and dispersal of the Golgi apparatus by *S. aureus* EV-mediated infection, consistent with STORM images.

Such fragmentation and dispersal of the Golgi apparatus may be related to disruption of the microtubule network. The Golgi apparatus, which is located near the nucleus, is known to be associated with the microtubule organizing center (MTOC). In diseased cells, especially those undergoing stress or transformation, such as cancer, the microtubule network can be disrupted, which leads to fragmentation and dispersal of the Golgi apparatus [40, 41]. To examine this relationship, we additionally performed STORM imaging of the MTOC by labeling acetylated tubulin. Interestingly, we observed a disrupted microtubule organizing center in *S. aureus* EV-infected HaCaT cells with a perturbed microtubule network, which was not observed in *S. epidermidis* EV-infected cells (Fig. 4D, Fig. S7). In particular, microtubule depolymerization and detachment from MTOC were observed in the quantitative analysis of MTOC from STORM images, probably suggesting Golgi fragmentation in response to microtubule depolymerization (Fig. 4E). Therefore, these findings indicate the disruptive potential of *S. aureus* EVs on cellular organelle integrity again, further implicating the pathogenicity of *S. aureus* EVs.

The investigation on toxic components in *S. aureus* EVs

Collectively, we could observe the pathogenic effect of *S. aureus* EVs on host cells, in contrast to *S. epidermidis* EVs (Fig. 5A). To investigate the distinct components in *S. aureus* EVs compared to *S. epidermidis* EVs that can induce harmful effects on host cells, we next performed STORM imaging of toxic components of EVs, including enterotoxin B and protein A. As shown in Fig. 5B-C, we observed that *S. aureus* EVs contain a higher amount of enterotoxin B and protein A, which could probably result in the harmful effect on the host cell. To further investigate this pathogenic effect, we also treated the HaCaT cells with purified protein A and performed STORM imaging of mitochondria, ER, and Golgi in these cells, in the same way to the *S. aureus* EV-treated cells. Remarkably, we observed similar ultrastructural alterations in host cells upon protein A treatment, as shown in Fig. 5D. In particular, mitochondrial fission, transformation of ER

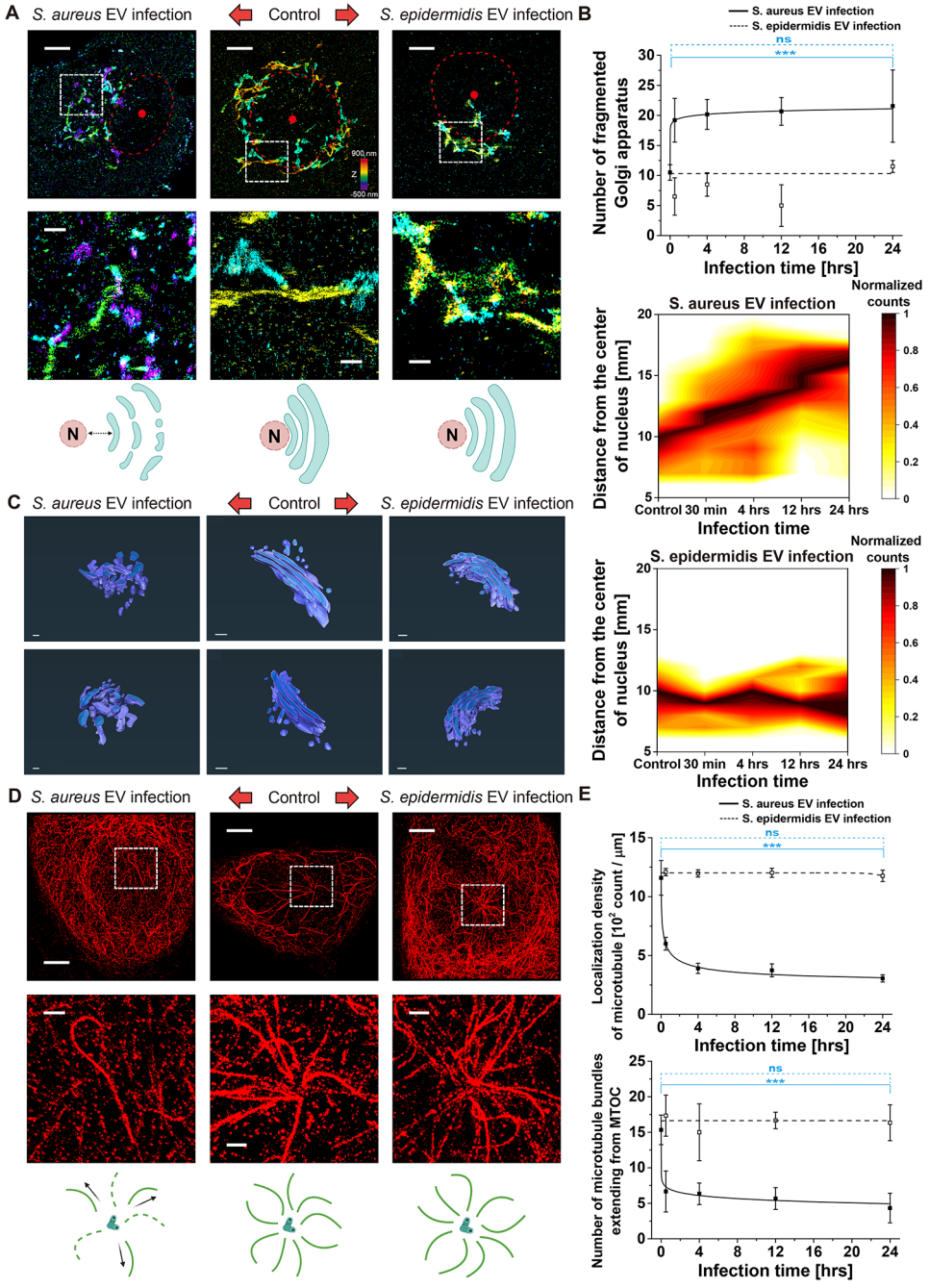

Fig. 4 Golgi dispersion and fragmentation by *S. aureus* EV infection. (**A**) Representative STORM images of the Golgi apparatus in epithelial keratinocyte (HaCaT) cells treated with *S. aureus* EVs (left) or *S. epidermidis* EVs (right) after 30 min of EV infection. Enlargement of the boxed region is shown at the bottom. Schematic diagrams are shown together. Red dashed line: nucleus boundary. (**B**) Quantitative analysis of the ultrastructural changes of the Golgi apparatus in terms of the number of Golgi fragments and the radial distribution from the center of the nucleus. ($n = 10$, mean ± SD) (**C**) 3D reconstructed HVEM images of HaCaT cells treated with *S. aureus* (left) or *S. epidermidis* (right) EVs after 30 min of EV infection at different angles, showing the fragmentation and dispersal of the Golgi apparatus by *S. aureus* EV infection. (**D**) Representative STORM images of acetylated tubulin to reveal the microtubule organizing center (MTOC) in HaCaT cells treated with *S. aureus* EVs (left) or *S. epidermidis* EVs (right). Enlargement of the boxed region is shown together at the bottom. (**E**) Quantitative analysis of the ultrastructural changes of the MTOC in terms of localization density and number of acetylated microtubule bundles extending from MTOC from STORM images, showing depolymerized MTOC by *S. aureus* EV infection. ($n = 10$, mean ± SD) (ns: $p > 0.05$, ***$p < 0.001$) Scale bars: (**A**) 5 μm (top), 1 μm (bottom), (**C**) 100 nm, (**D**) 5 μm (top), 1 μm (bottom)

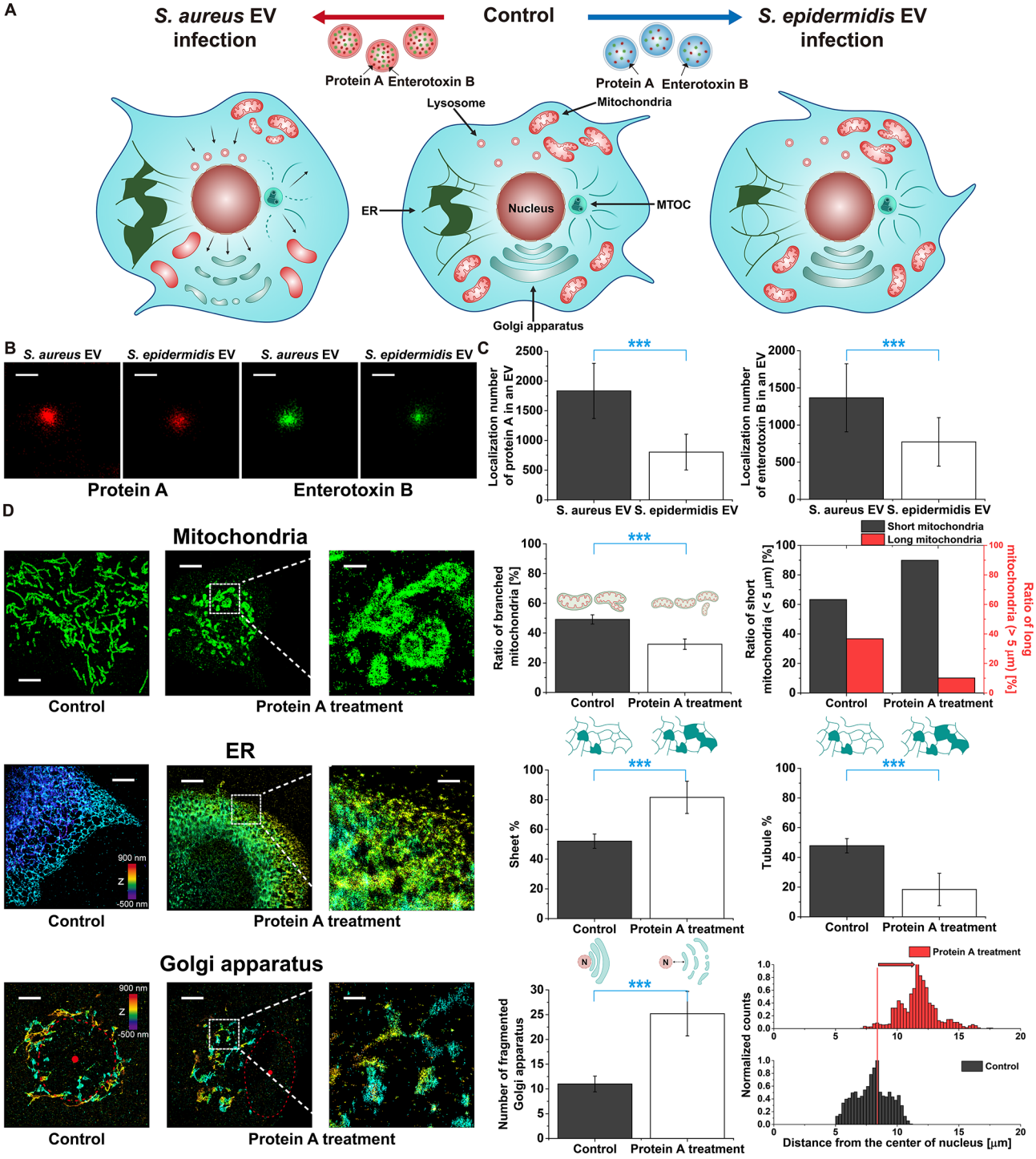

Fig. 5 Toxic components in *S. aureus* EVs that can induce harmful effects on host cells. (**A**) Bacterial EV type-dependent ultrastructural changes in host cell organelles after EV infection, implying the pathogenic effects of *S. aureus* EVs, in contrast to those of *S. epidermidis* EVs. (**B**) Representative STORM images of the EVs immunolabeled for protein A and enterotoxin B. (**C**) The quantitative analysis for the amount of the protein A and enterotoxin B in single EV. ($n = 10$, mean ± SD) (**D**) Representative STORM images and quantitative analysis of mitochondria, ER, and Golgi apparatus in HaCaT cells treated with protein A. (ns: $p > 0.05$, ***$p < 0.001$) Scale bars: (**B**) 100 nm, (**D**) 5 μm (left, middle), 1 μm (right)

from tubule to sheet structure, and dispersed and fragmented Golgi were observed in protein A-treated HaCaT cells, similar to the *S. aureus* EV-infected HaCaT cells. Therefore, it appears that protein A in *S. aureus* is mainly responsible for the observed ultrastructural disruption in *S. aureus* EV-infected cells. Protein A, also known as Staphylococcal protein A, is a well-known virulence factor found in *S. aureus*. It has been known that this surface protein can also be present in *S. aureus*-derived EVs. Since protein A plays a significant role in the pathogenesis of *S. aureus* infections by interacting with the host immune system, our observations support the idea that *S. aureus* can induce a response in the host immune system through EV-mediated protein A transportation. Moreover, our observation of the ultrastructural alteration caused by protein A can also support the previously reported observation of protein A-dependent changes in actin organization and tight junctions [42].

As other component candidates that can affect host cells, several toxic proteins have been reported, including α-hemolysin and enterotoxin [43–45]. Although we could not test the direct effects of these toxic candidates on host cells due to their commercial unavailability, they have also been known to induce cellular stress and even apoptosis. In particular, it has been reported that α-toxin induces apoptosis through the mitochondrial death pathway, which is associated with the loss of mitochondrial transmembrane potential [46]. Such a change in mitochondrial transmembrane potential appears to be related to our observation of cristae loss and mitochondrial fission induced by *S. aureus* EVs. Additionally, enterotoxin B has been reported to induce ER stress response, which is related to chronic inflammation [47]. Since we observed a higher level of enterotoxin B in *S. aureus* EVs compared to that in *S. epidermidis* EVs by STORM imaging, enterotoxin B is highly likely to induce the observed ER transformation from a tubular to a sheet-like structure. Therefore, these previous studies and our investigation of toxic components support the notion that *S. aureus* EVs can induce inflammation and associated ultrastructural changes in organelles through the delivery of toxic components.

Discussion

Our study provides novel insights into the ultrastructural alterations induced in host cells upon infection with EVs from both pathogenic *S. aureus* and less pathogenic *S. epidermidis*. The employment of advanced microscopic techniques, such as STORM and HVEM, allowed us to discern nanoscale changes in the mitochondrial, ER, and Golgi apparatus structures, revealing significant differences in the host cell responses to EVs from these two bacterial species in a concentration-dependent manner (Fig. S8). Although conventional microscopy can provide an overview of cellular structures, the nanoscale precision of STORM is crucial for the quantitative analyses central to our study. Subtle structural changes, particularly those in response to EV treatment, are only discernible and quantifiable using super-resolution techniques (Fig. S9). In particular, pronounced mitochondrial fission was observed in cells infected with *S. aureus* EVs, consistent with previous studies indicating that mitochondrial fragmentation is a hallmark of cellular stress and disease states, including viral infections [32, 33]. Also, the degraded cristae were observed in *S. aureus* EV-infected cells, indicating a disruption of energy homeostasis in host cells. Given the critical role of mitochondria in energy metabolism and signaling, these alterations could have profound implications for cell fate and function, potentially leading to cell death or dysfunction, thereby contributing to the pathogenicity of *S. aureus*. For example, the observed mitochondrial fission and loss of cristae could be indicative of an attempt by the host cell to isolate and remove damaged mitochondria, or it could reflect a strategy employed by the pathogen to manipulate host cell energy production and induce cell death. In addition, a shift from tubular to sheet-like ER structures was observed upon *S. aureus* EV infection, suggesting a stress response, possibly akin to autophagy under nutrient-depleted conditions [38]. The observed accumulation of lysosomes in the perinuclear regions reinforces this hypothesis, indicating the potential of ER morphology as a marker of bacterial EV-mediated cellular stress and pathogenicity. Finally, the Golgi apparatus in *S. aureus* EV-infected cells revealed fragmentation and dispersal, thus serving as indicators of cellular disarray and stress reminiscent of the changes observed in cells infected with viruses or undergoing transformation [39]. The potential link to microtubule network disruption suggests a broader impact of bacterial EVs on cellular architecture and integrity. These transformations of ER and Golgi morphology may interfere with protein synthesis and trafficking, thereby further impairing cell function and the immune response. For instance, ER and Golgi restructuring may be part of the unfolded protein response and autophagy, respectively, suggesting that cells attempt to respond to stress induced by pathogenic bacterial EVs by modulation of their intracellular architecture. This adaptive response, while potentially protective, may also contribute to disease pathology if overwhelmed or manipulated by the pathogenic factors contained in EVs. We observed that there is a high amount of protein A and enterotoxin B in *S. aureus* EVs compared to *S. epidermidis* EVs, as the distinct pathogenic factors in *S. aureus* EVs, which appear to be mainly responsible for inducing the observed destructive ultrastructural changes in organelles in host cells, including mitochondria, ER, and the Golgi apparatus. Interestingly,

such destructive changes of organelles were shown within an hour, suggesting that the pathogenic factors from bacterial EVs can be quickly delivered to the host cells. While our current study focused on fixed cells due to photobleaching constraints, future work employing long-term live-cell imaging techniques could potentially provide valuable insights into the early stages and dynamic progression of cellular responses to EV infection.

Collectively, these changes imply that *S. aureus* EVs induce a considerable stress response in skin cells, potentially leading to cell damage or death through mechanisms involving mitochondrial dysfunction, ER stress, and disruptions in protein processing and trafficking. This could contribute to the pathogenic effects of *S. aureus* on the skin, including inflammation, infection, or tissue damage. Since *S. aureus* is known to be involved in various skin conditions, such as impetigo, folliculitis, and more serious infections like cellulitis or abscesses, these observations suggest that *S. aureus* EVs could play a significant role in the pathogenesis of these conditions by directly inducing cellular dysfunction and death. Interestingly, we were also able to observe similar nanoscale changes in mitochondrial, ER, and Golgi apparatus structures in human dermal fibroblasts, indicating a conserved mechanism of EV-mediated intercellular communication across different skin cell types (Fig. S10). These findings suggest that bacterial EVs can universally influence skin cell biology, regardless of cell-specific functions or lineage. This conserved response among skin cells highlights the significance of bacterial EVs in the dermal microenvironment, suggesting that their effects extend beyond the infection site, potentially affecting skin homeostasis and integrity. This consistency across cell types highlights the potential of bacterial EVs as targets for developing diagnostic and therapeutic strategies. By documenting the specific ultrastructural changes induced by bacterial EVs, the progression of bacterial infections can be predicted and interventions designed that specifically target these pathogenic mechanisms.

Conclusions

In conclusion, our findings underscore the complexity of bacterial EV-mediated interactions with host cells and highlight the importance of understanding these processes in the context of bacterial pathogenesis. While our study illuminates the critical aspects of bacterial EV-mediated pathogenesis, further research is necessary to elucidate the specific molecular mechanisms underlying the observed ultrastructural changes. For example, exploring the host cell signaling pathways affected by bacterial EVs will deepen the understanding of the cellular response to bacterial invasion and potentially uncover novel interventional strategies. We expect that the distinct ultrastructural changes induced by pathogenic versus less pathogenic bacterial EVs will provide a foundation for the development of diagnostic tools and therapeutic strategies. Novel therapeutic approaches can be devised to mitigate the adverse effects of bacterial infections by targeting specific mechanisms through which pathogenic bacterial EVs disrupt host cell structures. Additionally, the differential effects of bacterial EVs on host cell ultrastructure could serve as biomarkers for early detection of bacterial infections, thereby enabling timely and targeted therapeutic interventions.

Supplementary Information

The online version contains supplementary material available at https://doi.org/10.1186/s12951-024-02817-6.

Supplementary Material 1

Supplementary Material 2

Supplementary Material 3

Supplementary Material 4

Supplementary Material 5

Supplementary Material 6

Supplementary Material 7

Author contributions

M. Kang and M.J. Kim performed research and analyzed data. D. Jeong, U. Jeong, N.G.Kang, S.J.Hwang, S.H.Youn, and B.K.Hwang reviewed the manuscript. H-J. Lim, G. Go, E. Moon, and H-S. Kweon performed research. D.Kim designed research, performed research, wrote the paper, and reviewed the manuscript.

Funding

This study was supported by National Research Foundation of Korea (NRF) Grant funded by the Korea government (MSIT) (no. 2021R1C1C1006700), the Future Cosmetics Research Support Program through the LG H&H Future Cosmetics Support Foundation (LG FCSF) funded by LG H&H, Korea Toray Science Foundation (2023), and the Korea Basic Science Institute under the R&D program (Project No. C330430) supervised by the Ministry of Science and ICT.

Data availability

No datasets were generated or analysed during the current study.

Declarations

Competing interests

The authors declare no competing interests.

Received: 22 May 2024 / Accepted: 30 August 2024
Published online: 06 September 2024

References

1. Deatherage BL, Cookson BT. Membrane vesicle release in bacteria, eukaryotes, and archaea: a conserved yet underappreciated aspect of microbial life. Infect Immun. 2012;80:1948–57.
2. Brown L, Wolf JM, Prados-Rosales R, Casadevall A. Through the wall: extracellular vesicles in Gram-positive bacteria, mycobacteria and fungi. Nat Rev Microbiol. 2015;13:620–30.
3. Kim JH, Lee J, Park J, Gho YS. Gram-negative and Gram-positive bacterial extracellular vesicles. In Seminars in cell & developmental biology. Elsevier; 2015: 97–104.

4. Ñahui Palomino RA, Vanpouille C, Costantini PE, Margolis L. Microbiota–host communications: bacterial extracellular vesicles as a common language. PLoS Pathog. 2021;17:e1009508.
5. Liu Y, Defourny KA, Smid EJ, Abee T. Gram-positive bacterial extracellular vesicles and their impact on health and disease. Front Microbiol. 2018;9:385261.
6. Kim MR, Hong SW, Choi EB, Lee WH, Kim YS, Jeon S, Jang M, Gho Y, Kim YK. S taphylococcus aureus-derived extracellular vesicles induce neutrophilic pulmonary inflammation via both T h1 and T h17 cell responses. Allergy. 2012;67:1271–81.
7. Brown L, Kessler A, Cabezas-Sanchez P, Luque-Garcia JL, Casadevall A. Extracellular vesicles produced by the G ram-positive bacterium B acillus subtilis are disrupted by the lipopeptide surfactin. Mol Microbiol. 2014;93:183–98.
8. Hong S-W, Choi E-B, Min T-K, Kim J-H, Kim M-H, Jeon SG, Lee B-J, Gho YS, Jee Y-K, Pyun B-Y. An important role of α-hemolysin in extracellular vesicles on the development of atopic dermatitis induced by Staphylococcus aureus. PLoS ONE. 2014;9:e100499.
9. Thay B, Wai SN, Oscarsson J. Staphylococcus aureus α-toxin-dependent induction of host cell death by membrane-derived vesicles. PLoS ONE. 2013;8:e54661.
10. Wang X, Thompson CD, Weidenmaier C, Lee JC. Release of Staphylococcus aureus extracellular vesicles and their application as a vaccine platform. Nat Commun. 2018;9:1379.
11. MUSHER DM, McKENZIE SO. Infections due to Staphylococcus aureus. Medicine. 1977;56:383–410.
12. Hell SW, Wichmann J. Breaking the diffraction resolution limit by stimulated emission: stimulated-emission-depletion fluorescence microscopy. Opt Lett. 1994;19:780–2.
13. Betzig E, Patterson GH, Sougrat R, Lindwasser OW, Olenych S, Bonifacino JS, Davidson MW, Lippincott-Schwartz J, Hess HF. Imaging intracellular fluorescent proteins at nanometer resolution. Sci. 2006;313:1642–5.
14. Jeong D, Kim D. Recent developments in correlative super-resolution fluorescence microscopy and electron microscopy. MOL CELLS. 2022;45:41–50.
15. Rust MJ, Bates M, Zhuang X. Sub-diffraction-limit imaging by stochastic optical reconstruction microscopy (STORM). Nat Methods. 2006;3:793–6.
16. Kim D, Deerinck TJ, Sigal YM, Babcock HP, Ellisman MH, Zhuang X. Correlative stochastic optical reconstruction microscopy and electron microscopy. PLoS ONE. 2015;10:e0124581.
17. French JB, Jones SA, Deng H, Pedley AM, Kim D, Chan CY, Hu H, Pugh RJ, Zhao H, Zhang Y. Spatial colocalization and functional link of purinosomes with mitochondria. Sci. 2016;351:733–7.
18. Chan CY, Pedley AM, Kim D, Xia C, Zhuang X, Benkovic SJ. Microtubule-directed transport of purine metabolons drives their cytosolic transit to mitochondria. PNAS. 2018;115:13009–14.
19. Katayama H, Hama H, Nagasawa K, Kurokawa H, Sugiyama M, Ando R, Funata M, Yoshida N, Homma M, Nishimura T. Visualizing and modulating mitophagy for therapeutic studies of neurodegeneration. Cell. 2020;181:1176–87. e1116.
20. Chen J, Stephan T, Gaedke F, Liu T, Li Y, Schauss A, Chen P, Wulff V, Jakobs S, Jüngst C. An aldehyde-crosslinking mitochondrial probe for STED imaging in fixed cells. PNAS. 2024;121:e2317703121.
21. Jeong D, Kim MJ, Park Y, Chung J, Kweon H-S, Kang N-G, Hwang SJ, Youn SH, Hwang BK, Kim D. Visualizing extracellular vesicle biogenesis in gram-positive bacteria using super-resolution microscopy. BMC Biol. 2022;20:270.
22. Chung J, Jeong U, Jeong D, Go S, Kim D. Development of a new approach for low-laser-power super-resolution fluorescence imaging. Anal Chem. 2021;94:618–27.
23. Huang B, Wang W, Bates M, Zhuang X. Three-dimensional super-resolution imaging by stochastic optical reconstruction microscopy. Sci. 2008;319:810–3.
24. Ester M, Kriegel H-P, Sander J, Xu X. A density-based algorithm for discovering clusters in large spatial databases with noise. In kdd. 1996: 226–231.
25. Levet F, Hosy E, Kechkar A, Butler C, Beghin A, Choquet D, Sibarita J-B. SR-Tesseler: a method to segment and quantify localization-based super-resolution microscopy data. Nat Methods. 2015;12:1065–71.
26. Chaudhry A, Shi R, Luciani DS. A pipeline for multidimensional confocal analysis of mitochondrial morphology, function, and dynamics in pancreatic β-cells. Am J Physiol Endocrinol Metab. 2020;318:E87–101.
27. Pain C, Kriechbaumer V, Kittelmann M, Hawes C, Fricker M. Quantitative analysis of plant ER architecture and dynamics. Nat Commun. 2019;10:984.
28. Nieuwenhuizen RP, Lidke KA, Bates M, Puig DL, Grünwald D, Stallinga S, Rieger B. Measuring image resolution in optical nanoscopy. Nat Methods. 2013;10:557–62.
29. Zaborowska M, Vazirisani F, Shah FA, Firdaus R, Omar O, Ekström K, Trobos M, Thomsen P. Immunomodulatory effects exerted by extracellular vesicles from Staphylococcus epidermidis and Staphylococcus aureus isolated from bone-anchored prostheses. Biomater. 2021;278:121158.
30. Kim MJ, Park J, Kang M, Jeong U, Jeong D, Kang N-G, Hwang SJ, Youn SH, Hwang BK, Hyun Y. Bacteria detection and species identification at the single-cell level using super-resolution fluorescence imaging and AI analysis. Biosens Bioelectron. 2023;240:115603.
31. Ma K, Chen G, Li W, Kepp O, Zhu Y, Chen Q. Mitophagy, mitochondrial homeostasis, and cell fate. Front cell dev biol. 2020;8:467.
32. Prahl S, Kueper T, Biernoth T, Wöhrmann Y, Münster A, Fürstenau M, Schmidt M, Schulze C, Wittern KP, Wenck H. Aging skin is functionally anaerobic: importance of coenzyme Q10 for anti aging skin care. BioFactors. 2008;32:245–55.
33. Mellem D, Sattler M, Pagel-Wolff S, Jaspers S, Wenck H, Rübhausen MA, Fischer F. Fragmentation of the mitochondrial network in skin in vivo. PLoS ONE. 2017;12:e0174469.
34. Gravel S-P, Khalifa YB, McGuirk S, St-Louis C, Laurin KM, Lavallée É, Benas D, Desbouis S, Amaral F, D'Amours D. PGC-1s shape epidermal physiology by modulating keratinocyte proliferation and terminal differentiation. Iscience 2023, 26.
35. Chung J, Jeong D, Kim G-h, Go S, Song J, Moon E, Huh YH, Kim D. Super-resolution imaging of platelet-activation process and its quantitative analysis. Sci Rep. 2021;11:10511.
36. Go S, Jeong D, Chung J, Kim G-h, Song J, Moon E, Huh YH, Kim D. Super-resolution imaging reveals cytoskeleton-dependent organelle rearrangement within platelets at intermediate stages of maturation. Struct. 2021;29:810–22. e813.
37. Lu M, Christensen CN, Weber JM, Konno T, Läubli NF, Scherer KM, Avezov E, Lio P, Lapkin AA. Kaminski Schierle GS: ERnet: a tool for the semantic segmentation and quantitative analysis of endoplasmic reticulum topology. Nat Methods. 2023;20:569–79.
38. Lu M, van Tartwijk FW, Lin JQ, Nijenhuis W, Parutto P, Fantham M, Christensen CN, Avezov E, Holt CE, Tunnacliffe A. The structure and global distribution of the endoplasmic reticulum network are actively regulated by lysosomes. Sci Adv. 2020;6:eabc7209.
39. Zhang J, Kennedy A, Xing L, Bui S, Reid W, Joppich J, Ahat E, Rose M, Tang Q, Tai AW. SARS-CoV-2 triggers Golgi fragmentation via down-regulation of GRASP55 to facilitate viral trafficking. bioRxiv 2022.
40. Thyberg J, Moskalewski S. Role of microtubules in the organization of the golgi complex. Exp Cell Res. 1999;246:263–79.
41. Li J, Ahat E, Wang Y. Golgi structure and function in health, stress, and diseases. The Golgi Apparatus and Centriole: Functions, Interactions and Role in Disease 2019:441–485.
42. Soong G, Martin FJ, Chun J, Cohen TS, Ahn DS, Prince A. Staphylococcus aureus protein A mediates invasion across airway epithelial cells through activation of RhoA GTPase signaling and proteolytic activity. JBC. 2011;286:35891–8.
43. Lee EY, Choi DY, Kim DK, Kim JW, Park JO, Kim S, Kim SH, Desiderio DM, Kim YK, Kim KP. Gram-positive bacteria produce membrane vesicles: proteomics-based characterization of Staphylococcus aureus-derived membrane vesicles. Proteomics. 2009;9:5425–36.
44. Gurung M, Moon DC, Choi CW, Lee JH, Bae YC, Kim J, Lee YC, Seol SY, Cho DT, Kim SI. Staphylococcus aureus produces membrane-derived vesicles that induce host cell death. PLoS ONE. 2011;6:e27958.
45. Wang X, Koffi PF, English OF, Lee JC. Staphylococcus aureus extracellular vesicles: a story of toxicity and the stress of 2020. Toxins. 2021;13:75.
46. Haslinger B, Strangfeld K, Peters G, Schulze-Osthoff K, Sinha B. Staphylococcus aureusα-toxin induces apoptosis in peripheral blood mononuclear cells: role of endogenous tumour necrosis factor-α and the mitochondrial death pathway. Cell Microbiol. 2003;5:729–41.
47. Kim Y-M, Jin J, Choi J-A, Cho S-N, Lim Y-J, Lee J-H, Seo JY, Chen HY, Rha K-S, Song C-H. Staphylococcus aureus enterotoxin B-induced endoplasmic reticulum stress response is associated with chronic rhinosinusitis with nasal polyposis. Clin Biochem. 2014;47:96–103.

Publisher's note